ACS Catalysis

RESEARCH ARTICLE

pubs.acs.org/acscatalysis

Carbon Nanotube-Supported RuFe Bimetallic Nanoparticles as Efficient and Robust Catalysts for Aqueous-Phase Selective Hydrogenolysis of Glycerol to Glycols

Bodong Li,[†] Juan Wang,[†] Youzhu Yuan,[*,†] Hiroko Ariga,[‡] Satoru Takakusagi,[‡] and Kiyotaka Asakura[*,‡]

[†]State Key Laboratory of Physical Chemistry of Solid Surfaces, National Engineering Laboratory for Green Chemical Productions of Alcohols-Ethers-Esters, College of Chemistry and Chemical Engineering, Xiamen University, Xiamen 361005, China

[‡]Catalysis Research Center, Hokkaido University, Kita-ku N21W10, Sapporo, Hokkaido 001-0021, Japan

Supporting Information

ABSTRACT:

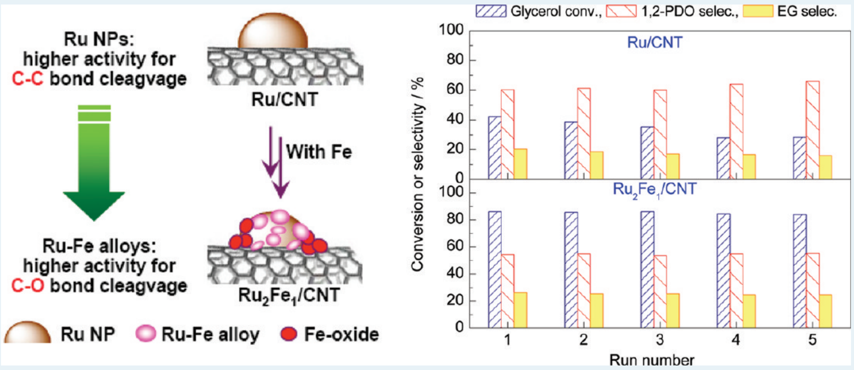

Carbon nanotube-supported RuFe bimetallic catalysts (RuFe/CNT) were prepared through a coimpregnation method for the selective hydrogenolysis of 20 wt % glycerol aqueous solution to produce glycols (1,2-propanediol and ethylene glycol). The Ru/CNT catalyst with smaller Ru nanoparticles (NPs) was significantly active for C−C bond cleavage, giving a considerable amount of CH_4 in the hydrogenolysis product. The RuFe/CNT catalyst with bimetallic NPs having an average size similar to Ru/CNT was more efficient for C−O bond cleavage, affording higher selectivity to glycols. Almost 100% glycerol conversion and over 75% selectivity to glycol could be obtained using the optimized RuFe/CNT catalyst under relatively mild conditions. The bimetallic RuFe/CNT catalyst was structurally robust and showed excellent reusability. Transmission electron microscopic images revealed that, when an appropriate amount of Fe entity was added, the RuFe bimetallic NPs were uniformly dispersed on the CNT surfaces and had an average size of ∼3 nm. X-ray photoelectron spectroscopy indicated that a portion of the Fe species were interacted with Ru moieties, forming Ru−Fe alloys on the Ru domain, whereas other Fe species were in the forms of iron oxides, likely FeO and FeO_{1+x} $(0 < x < 0.5)$, mostly presenting on the periphery of RuFe bimetallic NPs. The occurrence of iron oxide species is crucial for the stability of RuFe bimetallic NPs during catalytic runs; but excess iron oxides block the surfaces of RuFe bimetallic NPs, resulting in a decrease in catalytic activity. Higher performance of the RuFe/CNT catalyst is attributed to the synergistic effects of the formation of Ru−Fe alloys and the interactions between the RuFe bimetallic NPs and iron oxides on CNT surfaces.

KEYWORDS: Glycerol, Hydrogenolysis, Carbon nanotube, Bimetallic catalyst, Ru−Fe alloy, Glycol

INTRODUCTION

Because of its ample availability as a byproduct of biodiesel production,[1] glycerol is considered one of the top 12 building blocks of biorefinery.[2] New applications of glycerol will inevitably benefit the economy of the whole biodiesel production industry. In fact, glycerol has served as a model molecule that not only allows the exploration of its conversion to H_2 and CO_2 but also its transformation into valuable commodity chemicals. Among these, the catalytic hydrogenolysis of glycerol has attracted much attention for the production of glycols such as propanediols (1,2-PDO and 1,3-PDO) and ethylene glycol (EG).[3]

A number of heterogeneous catalysts, including Cu-based,[4−6] Ni-based,[7,8] and Ru-based catalysts,[9−13] and other noble metal (Rh, Pt, and Au) catalysts[14−16] have been employed for the hydrogenolysis of glycerol to PDOs and EG. Ruthenium has long been considered as one of the effective catalyst components of glycerol hydrogenolysis. However, several studies have showed that the activity and selectivity for glycerol hydrogenolysis of Ru

Received: July 25, 2011
Revised: September 6, 2011
Published: September 26, 2011

catalysts alone were not sufficient. Modifying Ru catalysts to improve their performance in the hydrogenolysis of glycerol has been proposed. Miyazawa et al. reported that in comparison with the combinations of other noble metal catalysts (Rh/C, Pt/C, and Pd/C) and acid promoters (Amberlyst resins, H_2SO_4, and HCl), combining Ru/C and Amberlyst resin was the most effective for the hydrogenolysis of glycerol to 1,2-PDO.[10] Some base additives such as NaOH and CaO could increase the activity of Ru/C and Pt/C catalysts.[16] Ma et al. discovered a remarkable promoting effect of the Re component on the activity of Ru catalysts in the hydrogenolysis of glycerol to PDOs.[17] Modification of supported Rh and Ir catalysts with ReO_x were considerably effective at converting aqueous glycerol to more valuable 1,3-PDO.[18−23] It has also been reported that bimetallic catalysts are superior to monometallic catalysts in terms of catalytic activity and selectivity for many reactions.[24] Maris et al. applied bimetallic PtRu/C and AuRu/C catalysts to the hydrogenolysis of glycerol and found that PtRu was more stable than Ru/C under aqueous-phase reaction conditions, although the activity and selectivity of PtRu/C was similar to its monometallic Ru/C counterpart.[15,16]

A previous study revealed that Ru nanoparticles supported on multiwall carbon nanotubes (Ru/CNT) had a higher performance in the hydrogenolysis of glycerol to produce glycols of 1,2-PDO and EG in comparison with catalysts supported on other carriers.[25] Glycerol conversion and product selectivity depended essentially on the mean size of the Ru nanoparticles (Ru NPs). Ru mean size ∼ 5 nm produced the highest glycol yield. However, selectivities to glycols dropped when glycerol conversion was higher than 80%, since agglomeration and coagulation of Ru NPs occurred considerably in the process of hydrogenolysis. The present work discusses the remarkable promoting effect of Fe species on the performance of Ru/CNT catalysts for the hydrogenolysis of glycerol to 1,2-PDO and EG. The structure−activity relationship of the RuFe/CNT catalyst is also discussed on the basis of characteristic studies through various techniques.

EXPERIMENTAL SECTION

2.1. Catalyst Preparation. CNTs of outer diameter 10−60 nm were prepared by the catalytic decomposition of CH_4.[26] As-received raw CNT was purified in concentrated HNO_3 at 353 K for 16 h to remove residual contaminants and amorphous carbon. Analysis using inductively coupled plasma optical emission spectrometry (ICP-OES) using a Thermo Electron IRIS Intrepid II XSP showed that the remaining Ni impurity in CNT was less than 0.006 wt %. Monometallic catalysts were prepared by impregnation of the supports with an aqueous solution of $RuCl_3 \cdot 3H_2O$. Bimetallic RuFe catalysts were prepared through a coimpregnation method using aqueous solutions of $RuCl_3 \cdot 3H_2O$ and $Fe(NO_3)_3 \cdot 9H_2O$. The Ru loading weight was kept constant at 5 wt %, and the Ru/Fe atomic ratio was varied accordingly. After impregnation and solvent removal by evaporation, the produced solids were dried overnight at 383 K. All dry samples were calcined at 673 K for 4 h in air. Prior to reaction, the samples were reduced by 5% H_2/95% N_2 for 4 h at 723 K. The bimetallic catalyst was denoted as Ru_xFe_y/CNT, where x and y stand for the atomic ratios of Ru and Fe, respectively.

2.2. Catalyst Characterization. H_2-temperature-programmed reduction (H_2-TPR) profiles were measured in a fixed bed continuous flow reactor connected to a thermal conductivity detector (TCD). A 50 mg sample of the catalyst precursor was pretreated in Ar (30 mL/min) at 623 K for 30 min and then cooled to room temperature. Subsequently, reducing gas composed of 5% H_2/95% Ar was employed at a flow rate of 30 mL/min and a heating rate of 10 K/min from ambient to 1173 K. TCD monitored the H_2 consumption.

X-ray powder diffraction (XRD) patterns were measured on a Phillips Panalytical X'pert Pro diffractometer equipped with a graphite monochromator and Cu K_α radiation (40 kV and 30 mA). Diffraction data were collected by a continuous scan mode of scan speed 1° (2θ)/min.

XPS measurements were performed on a JPS-9010MC photoelectron spectrometer using an Al K_α (1486.6 eV) radiation source. The XPS spectra of as-calcined Fe/CNT and RuFe/CNT samples as well as those after in situ treatments in 100 Pa H_2 at 623 K for 4 h were recorded in an auxiliary reaction chamber. After treatment, the sample was introduced into the XPS chamber, avoiding exposure to air. To obtain the XPS spectra, pressure in the analysis chamber was maintained at 5×10^{-9} mbar. All spectra were recorded at room temperature, and the binding energy (BE) was set as 284.6 eV for C 1s. Peak deconvolution and fitting were performed using the peak-fitting software "SPECSURF, JEOL" with the spin−orbit splitting and the relative intensities of the spin−orbit components fixed.

Transmission electron microscopy (TEM) images and nanoscale elemental mappings were performed on a Tecnai F30 electron microscope operated at an acceleration voltage of 300 kV. Samples for TEM measurements were ultrasonically dispersed in ethanol. Drops of the suspension were deposited on a carbon-coated copper grid.

The Brunauer−Emmett−Teller surface area (S_{BET}) of the catalyst was measured by N_2 adsorption at 77 K with a Micrometrics Tristar 3020 instrument. Before the measurements, the samples were degassed at 573 K for 2 h. The dispersion of Ru metal was determined by H_2 and O_2 chemisorption according to the procedures described in literature.[27] The experiments were performed on a Micromeritics ASAP 2010 M+C instrument. The catalyst sample was first reduced with 5% H_2/95% Ar at 573 K for 1 h, followed by evacuation for 30 min. Then the sample was cooled to 308 K under vacuum for O_2 (99.999%) adsorption to form Ru_s−O species on the surface. After that, the H_2 adsorption was taken at 373 K to measure the amount of Ru_s−O species. The dispersion of metal Ru was calculated by assuming H/Ru_s = 3 stoichiometry due to the following reactions.

$$Ru_s + 1/2O_2 \rightarrow Ru_s - O \tag{1}$$

$$Ru_s - O + (3/2)H_2 \rightarrow Ru_s\text{-}H + H_2O \tag{2}$$

2.3. Catalytic Testing. Hydrogenolysis was performed in a 100 mL stainless steel autoclave at a stirring speed of 400 rpm. The reactor was purged with H_2 (99.99%), the system was then pressurized with H_2 to the designed pressure and, finally, heated to the reaction temperature. Thr temperature was monitored using a thermocouple inserted into the autoclave and connected to the thermocontroller. The standard reaction was carried out under the following conditions: 473 K, 4.0 MPa initial H_2 pressure, 20 mL 20 wt % glycerol aqueous solution, and 250 mg catalyst. After the reaction, the autoclave was placed in an ice−water bath, and the pressure was released carefully.

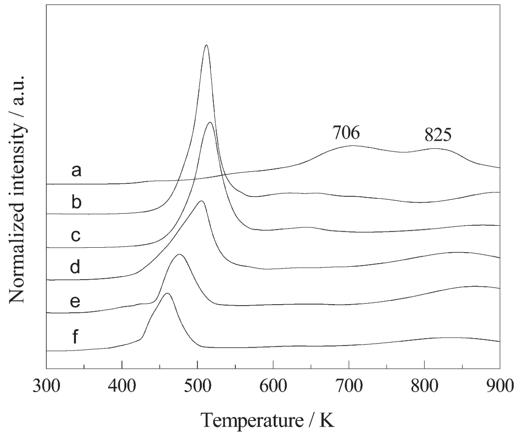

Figure 1. H_2-TPR profiles of several bimetallic RuFe/CNT catalysts with different Ru/Fe atomic ratios: (a) Fe/CNT, (b) Ru_1Fe_1/CNT, (c) Ru_2Fe_1/CNT, (d) Ru_4Fe_1/CNT, (e) $Ru_{10}Fe_1$/CNT, and (f) Ru/CNT.

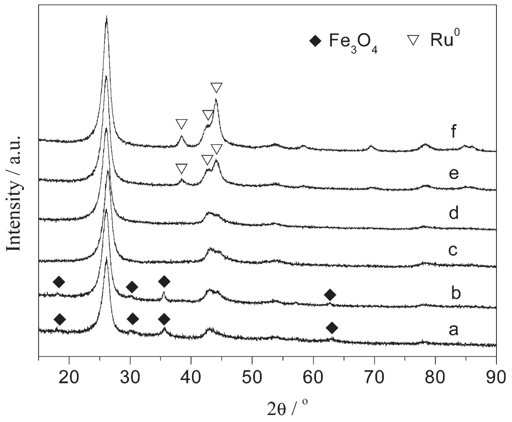

Figure 2. XRD patterns of several RuFe/CNT catalysts with different Ru/Fe atomic ratios: (a) Fe/CNT, (b) Ru_1Fe_1/CNT, (c) Ru_2Fe_1/CNT, (d) Ru_4Fe_1/CNT, (e) $Ru_{10}Fe_1$/CNT, and (f) Ru/CNT.

The gas-phase products were analyzed using an online gas chromatograph equipped with two TCDs and two columns of Porapak Q and Molsieve 5A. The liquid-phase products, after being separated from the catalyst powder by filtration, were analyzed using a gas chromatograph equipped with a flame ionization detector and a capillary column (KB-WAX, 30 m × 0.25 mm × 1.0 μm). A solution containing a known amount of 1,4-butanetiol was added as an internal standard for each analysis. The products were identified using authentic samples. In all cases, less than 2% 1,3-PDO was produced; it was therefore not listed in the following results. The conversion of glycerol and the selectivity of products were calculated by following equations:

$$\text{conversion } (\%) = \frac{\text{moles of glycerol consumed}}{\text{moles of glycerol initially charged}} \times 100\%$$

$$\text{selectivity } (\%) = \frac{\text{moles of carbon in specific product}}{\text{moles of carbon in all detected products}} \times 100\%$$

Glycol yield (1,2-PDO and EG) was calculated using the following equation:

$$\text{yield } (\%) = \text{conversion } (\%) \times \text{selectivity } (\%) \times 100\%$$

The turnover frequency (TOF) was based on the number of surface Ru metal atoms determined from the results of H_2 and O_2 chemisorption, indicating the moles of glycerol converted by per Ru atom at the catalyst surface per hour (mol-glycerol mol-$\text{Ru}_{\text{surf}}^{-1}$ h^{-1}, for short, h^{-1}). The glycerol conversion for the TOF calculation was around 50%.

■ RESULTS AND DISCUSSION

3.1. Catalyst Characterization. Figure 1 shows the H_2-TPR profiles of the as-calcined samples with different Ru/Fe atomic ratios by keeping Ru loading at 5.0 wt %. For the as-calcined 5.0 wt % Fe/CNT sample, two distinct peaks appeared in the TPR profile. The first peak at around 706 K was assigned to the reduction of iron oxide, and the second peak above 750 K was attributed to both iron oxide particles interacting with carbon as well as the possible gasification of CNT.[28] The as-calcined Ru/CNT sample presented a peak at about 450 K, assigned to the reduction of RuO_2. The presence of a noble metal is known to affect the reducibility of surfaces metal oxides and has been described to lower the reduction temperature of the oxide.[29,30] It has also been reported that close interaction between these two metal species could inhibit the reduction of the noble metal oxide.[30] The TPR curves obtained in the present study showed that when a small amount of Fe was added into the Ru/CNT system (e.g., Ru/Fe atomic ratio = 10/1), the H_2 consumption peak of the derived as-calcined sample shifted to higher temperature, in comparison with the RuO_2 reduction peak. With the increase in the Fe amounts, this peak shifted farther to higher temperatures, and its intensity became sharper. Therefore, some interactions between Ru and Fe species occurred. However, there were no significant differences between the H_2-TPR curves of Ru_2Fe_1/CNT and that of Ru_1Fe_1/CNT, implying that there was an appropriate Ru/Fe ratio in connection with their interaction.

The XRD patterns of the as-reduced RuFe/CNT catalysts with different Ru/Fe atomic ratios are shown in Figure 2. Distinct diffraction peaks of the metallic Ru species (2θ = 38.5°, 42.3°, and 44.0°) were observed in the XRD pattern of Ru/CNT. When a small amount of Fe was added to Ru/CNT, for example, by forming a sample of $Ru_{10}Fe_1$/CNT, the intensity of metallic Ru diffraction peaks decreased significantly, and no diffraction peaks ascribed to the Fe species were observed. When the Fe amount was further increased by forming the samples of Ru_4Fe_1/CNT and Ru_2Fe_1/CNT, no clear diffraction peaks assignable to Ru or Fe species could be clearly identified in their XRD patterns, mostly because of the limit of detection (<4 nm). However, as the Ru/Fe atomic ratio approached 1/1, the diffraction peaks owing to Fe_3O_4 (2θ = 15.3°, 30.1°, and 35.4°) appeared. The above results suggest that the addition of Fe to the Ru/CNT catalyst enables better dispersion of the metallic NPs on the CNT.

Characterization of XPS was performed to clarify the species of Ru and Fe before and after reduction. The Fe 2p and Ru 3p spectra of the Fe/CNT and Ru_1Fe_1/CNT samples are displayed in Figure 3, and those of the Ru_2Fe_1/CNT sample are depicted in Figure S1 in the Supporting Information. The XPS curve-fitting results are summarized in Table 1. It can be seen that the spectra of the Fe/CNT sample before and after reduction at 623 K were similar to each other (Figure 3A), showing a binding energy of

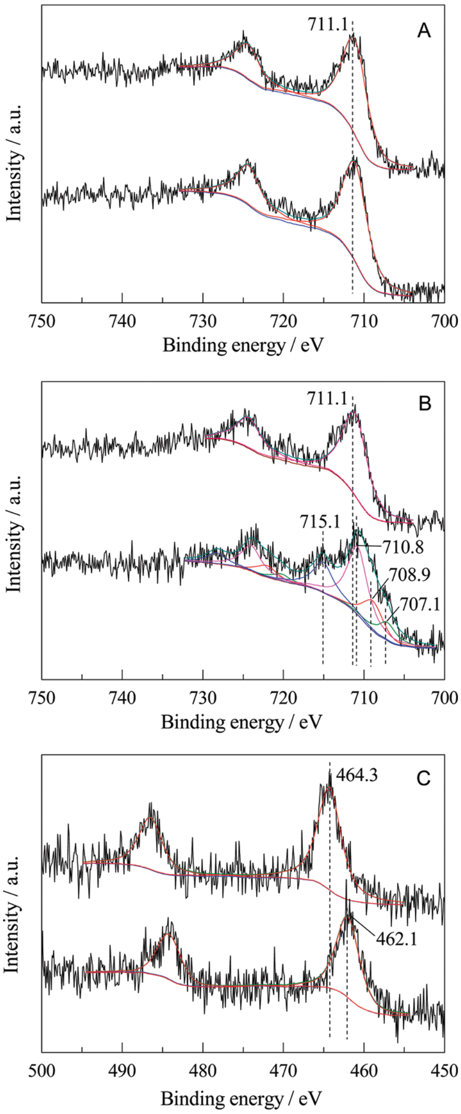

Figure 3. Fe 2p and Ru 4p XPS of Fe/CNT and RuFe/CNT catalysts before and after reduction: (A) Fe 2p spectra of Fe/CNT, (B) Fe 2p spectra of Ru_1Fe_1/CNT, and (C) Ru 3p spectra of Ru_1Fe_1/CNT.

Fe $2p_{3/2}$ at 711.1 eV, typical of Fe^{3+}. In other words, the Fe species on CNT were hardly reduced under the present conditions (623 K for 4 h). However, the XPS results of the Ru_1Fe_1/CNT sample indicated that the Fe 2p spectra changed significantly before and after reduction, as shown in Figure 3B. The binding energy of Fe $2p_{3/2}$ in the as-calcined Ru_1Fe_1/CNT was the same as in Fe/CNT, but it could be deconvoluted into three peaks at 710.8, 708.9, and 707.1 eV after H_2 reduction at 673 K for 4 h. In addition, there was a binding energy around 715.0 eV assignable to the satellite peak of the Fe^{2+} species, which is commonly observed in the XPS data of Fe^{2+} compound.[31]

We carried out the peak-fitting by fixing two peaks at 711.1 and 707.1 eV, but the fitting results became worse. The possible assignments for these three peaks are as follows: The peak at 707.1 eV was ascribed to the presence of metallic Fe species, the one at 710.8 eV was due to FeO, and the one at 708.9 eV was attributed to FeO_{1+x} ($0 < x < 0.5$). Thus, the Fe species were reduced into iron oxides with lower binding energies (BE for Fe $2p_{3/2}$ = 710.8 and 708.9 eV) and metallic Fe (BE = 707.1 eV) after the H_2 reduction. Similar fitting results were obtained for the Fe 2p spectrum of Ru_2Fe_1/CNT catalyst. On the other hand, the binding energy of Ru 3p was 462.1 and 484.3 eV in the reduced samples, lower than that of Ru 3p in the as-calcined samples (464.3 and 486.5 eV) (Figures 3C and Supporting Information S1-B), unquestionably confirming the transformation of Ru^{4+} to Ru^0 during the H_2 reduction.

The concentrations of metallic Fe in the samples of Ru_2Fe_1/CNT and Ru_1Fe_1/CNT after reduction were around 11.8% and 16.0%, respectively (Table 1). These metallic Fe species were assumed to interact with metallic Ru ones by formation of Ru−Fe alloys, and they were located on the Ru domain, whereas the iron oxides were present on the periphery of RuFe bimetallic NPs. Therefore, the results of XPS and XRD suggested that the Fe species were unable to be entirely reduced under the present conditions of 5% H_2/95% N_2 atmosphere, and there was a considerable amount of iron oxides, likely FeO and FeO_{1+x} (most possibly Fe_3O_4), remaining on the catalyst surfaces. Further, the amount of Ru−Fe alloy entities slightly increased with the increase of Fe loading.

Figure 4 shows the TEM images of the RuFe/CNT catalyst with different Ru/Fe ratios. The mean particle size of NPs

Table 1. Curve-Fitting Results of Fe 2p XPS of RuFe/CNT Catalysts

		before reduction[a]			after reduction[a]		
catalyst	species	BE_{Fe} $2p_{1/2}$	BE_{Fe} $2p_{3/2}$	concn, %	BE_{Fe} $2p_{1/2}$	BE_{Fe} $2p_{3/2}$	concn, %
5 wt % Fe/CNT	Fe^{3+}	724.4	711.1	100	724.3	711.1	100
	Fe^{2+}	ND	ND	0	ND	ND	0
	Fe	ND	ND	0	ND	ND	0
Ru_2Fe_1/CNT	Fe^{3+}	724.3	711.1	100	ND	ND	0
	FeO_{1+x}[b]	ND	ND	0	724.0	710.8	67.0
	Fe^{2+}	ND	ND	0	722.1	708.9	21.1
	Fe	ND	ND	0	720.3	707.1	11.8
Ru_1Fe_1/CNT	Fe^{3+}	724.3	711.1	100	ND	ND	0
	FeO_{1+x}	ND	ND	0	724.0	710.8	61.3
	Fe^{2+}	ND	ND	0	722.1	708.9	22.8
	Fe	ND	ND	0	720.3	707.1	16.0

[a] ND = not detected. [b] $0 < x < 0.5$.

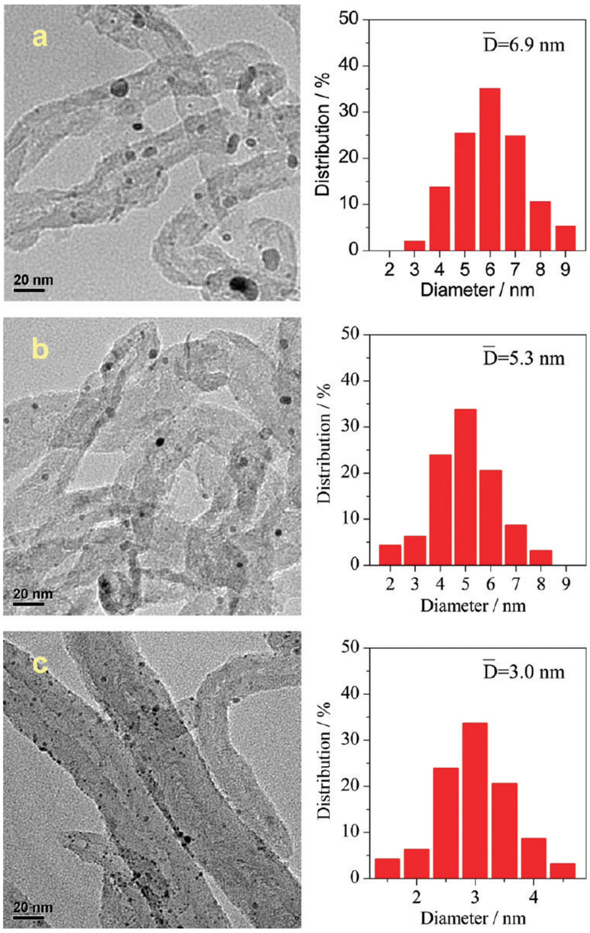

Figure 4. TEM micrographs and metallic particle size distributions of RuFe/CNT with different Ru/Fe atomic ratios: (a) as-prepared Ru/CNT, (b) as-prepared $Ru_{10}Fe_1$/CNT, and (c) as-prepared Ru_2Fe_1/CNT.

decreased from 6.9 to 5.3 nm when a small amount of Fe was added (Ru/Fe = 10/1). The particle size decreased with the increase in Fe loading, giving small and uniform NPs with an average particle size around 3.0 nm homogeneously distributed on the CNT surfaces. The representative HRTEM image of as-reduced Ru_1Fe_1/CNT catalyst as shown in Figure 5 indicated that the two intervals of 0.200 and 0.226 nm between the corresponding two lattice fringes were slightly smaller than the (101) and (100) lattice spacings of ruthenium in the Ru/CNT catalyst with $p6_3/mmc$ structure (Figure S2 in the Supporting Information), but larger than the (110) and (200) lattice spacings of iron with cubic Im_3m structure, respectively. The included angle around 25° of the two facets in the Ru_1Fe_1/CNT is very close to the theoretical value of 28.45° between the {100} and {101} facets, implying that the exposed crystal planes of the Ru_1Fe_1/CNT catalyst were dominated by {100} and {101} facets of Ru−Fe alloy. Nanoscale elemental mapping revealed that Fe was distributed throughout the entire Ru domain (Figure 5, inserts), suggesting that Ru and Fe were located at the same position. These indications strongly suggested the formation of Ru−Fe alloy in the Ru domain and other Fe-species on the periphery of RuFe bimetallic NPs.

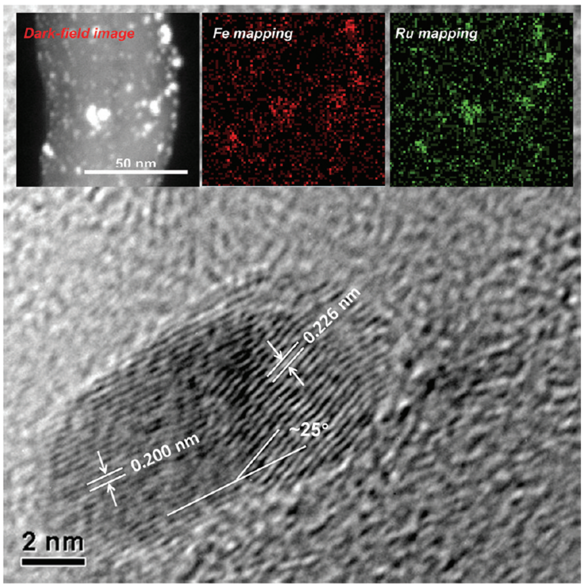

Figure 5. HRTEM image and nanoscale elemental mapping images (inserts) of Ru_1Fe_1/CNT catalyst.

Table 2. Physicochemical Characterization of Several Supported Ru Catalysts

		average size of Ru/nm		dispersion/%	
catalyst (Ru loading = 5 wt %)	S_{BET}, $m^2\ g^{-1}$	by TEM	by XRD	by TEM[a]	by H_2-O_2 titration
Ru_2Fe_1/AC[b]	498.1	4.6	4.9	28.7	19.8
Ru_2Fe_1/CNT	115.1	3.0		44.0	24.5
$Ru_{10}Fe_1$/CNT	110.5	5.3	4.4	30.0	25.4
Ru_4Fe_1/CNT	111.7	3.1		42.6	33.7
Ru_3Fe_1/CNT	105.2	3.2		41.3	31.2
Ru_1Fe_1/CNT	100.3	3.0		44.0	12.9
Ru/CNT-A	102.6	6.9	7.2	18.5	19.1
Ru/CNT-B	105.6	2.8		47.1	35.8

[a] All the Ru particles were regarded as the spheres. Thus, the Ru dispersion, D, was calculated as $D = (6v_m/a_m d) \times 100\%$, according to literature,[32] where, D is the Ru dispersion; v_m is the volume of a Ru atom, $v_m = (M/\rho N_o)$, M is the molecular weight of Ru, ρ is the density of Ru, N_o is Avogadro's constant; a_m is the area of a Ru atom on the surface, $a_m = 1/(1.63 \times 10^{19})$;[33] and d is the Ru particle diameter determined by TEM. Therefore, $D = 1.32/d$. [b] AC: Active carbon.

In addition, the TEM image of the RuFe/CNT catalyst after the glycerol reaction showed that the metal particle size was almost equal to that of the as-reduced RuFe/CNT one (Figure S3 in the Supporting Information). This equivalence indicated that high dispersion was maintained throughout the reaction. However, for the monometallic Ru catalyst used, the metal particles were agglomerated, and the size of Ru NPs increased to ~10.7 nm. These results suggest that the addition of Fe enables metallic particles to disperse better on the support and helps stabilize RuFe bimetallic NPs against agglomeration and sintering.

The physicochemical properties of several supported RuFe catalysts are listed Table 2. The S_{BET} data of the CNT-supported catalysts were very similar to each other, but much lower than that of the AC-supported one. The metal dispersion data by H_2

Table 3. Glycerol Hydrogenolysis over the RuFe/CNT Catalyst with Different Ru/Fe Atomic Ratios[a]

				Selec./%[c]				
catalyst (Ru loading = 5 wt %)	Ru NPs, nm[b]	time, h	conv, %	1,2-PDO	EG	CH_4	yield of glycols, %	TOF, h^{-1}
5 wt % Fe/CNT		12	2.8	64.3	20.9	2.1	2.4	
Ru/CNT-A	6.9	12	42.3	60.2	20.4	6.6	34.1	65.3
$Ru_{10}Fe_1$/CNT	5.3	12	57.7	45.4	30.7	13.4	43.9	69.0
Ru_2Fe_1/CNT	3.0	12	86.0	52.3	23.5	11.2	68.0	147.5
Ru_1Fe_1/CNT	3.0	12	57.1	61.4	19.3	7.3	46.1	134.4
Ru/CNT-B	2.8	6	64.5	22.1	30.1	32.9	24.3	106.2
Ru_4Fe_1/CNT	3.1	6	64.1	37.4	30.8	17.6	43.7	115.5
Ru_3Fe_1/CNT	3.2	6	56.4	46.3	29.8	13.0	42.9	124.3
Ru_2Fe_1/CNT	3.0	6	59.5	52.7	24.2	11.8	48.1	147.5
Ru_2Fe_1/AC	4.6	12	53.8	37.0	31.0	20.5	36.6	88.7

[a] Reaction conditions: catalyst amount = 250 mg; 20 wt % glycerol aqueous solution = 20 mL; H_2 pressure = 4.0 MPa; temp = 473 K; stirring speed = 500 rpm. [b] Average Ru particle size determined by TEM. [c] Others include 1-propanol, ethanol, 1,3-PDO, and CO_2.

and O_2 chemisorption were decreased with the increase in Fe content in the samples with almost the same TEM average particle size. In general, however, they were smaller than those estimated from the TEM average particle size,[32,33] particularly in the case of the sample with a lower Ru/Fe atomic ratio. The existence of Ru−Fe alloys may bring about some influences on the measurement of H_2 and O_2 chemisorption, but the lower metal dispersion data by this method are more likely due to the blockage of some iron oxide species to the surface of active sites as deduced by the results of XPS and nanoscale element mapping.

3.2. Catalytic Results. The performance of the RuFe/CNT catalysts on the hydrogenolysis of glycerol as a function of Ru/Fe atomic ratio is listed in Table 3. For conciseness, selectivities to the main products of 1,2-PDO, EG, and CH_4 are provided. Other products, such as 1-propanol, ethanol, 1,3-PDO, and CO_2, are present but have not been included in Table 3. The Ru/Fe atomic ratio had a significant effect on the conversion of glycerol. Over the Ru/CNT catalyst, the reaction gave a conversion of 42.3% with selectivity values of 60.2% and 20.4% to 1,2-PDO and EG, respectively. Fe/CNT presented almost negligible activity under the experimental conditions. When Fe was added into Ru/CNT, glycerol conversion increased with the increment of Fe amount in RuFe/CNT and reached a maximum (86.0%) at the Ru/Fe atomic ratio of 2/1. In the case of almost the same average size of metal NPs, the Ru/CNT catalyst exhibited higher Ru dispersion as compared with RuFe/CNT, but it gave a lower TOF. The Ru/CNT catalyst with a larger particle size could afford a higher selectivity to glycols, but it showed a significantly lower TOF.

The different performances over the monometallic and bimetallic catalysts could be most likely ascribed to their different surface structures. The formation of Ru−Fe alloys on the RuFe/CNT catalyst might be able to provide positive effects for the activations of substrate molecules, as reflected by the results that slightly increasing the amount of Ru−Fe alloy entities by the increase of Fe content could bring about a beneficial effect for the catalyst performance. For example, the bimetallic $Ru_{10}Fe_1$/CNT catalyst with an average size of metal NPs around 5.3 nm exhibited activity and selectivity close to those of the monometallic Ru/CNT one, with an average size of metal NPs around 6.9 nm, whereas the Ru_1Fe_1/CNT one performed at higher TOF and good selectivity to glycols. However, neither a large excess of Ru nor an excess of Fe in the RuFe/CNT catalyst exhibited superior performance for the hydrogenolysis of glycerol.

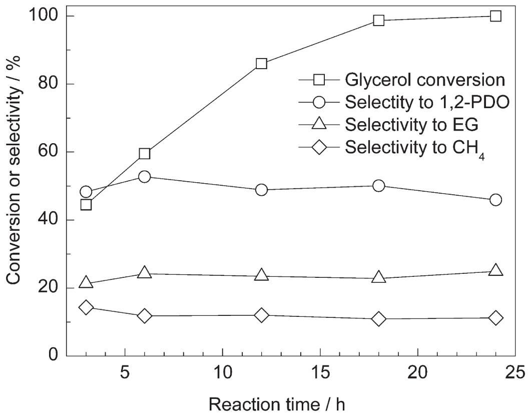

Figure 6. Glycerol conversion and product selectivity over Ru_2Fe_1/CNT catalyst as a function of reaction time. The reaction conditions are the same as in Table 3.

The previous work indicated that the glycerol conversion, product selectivities, and glycol yield depended on the average size of Ru NPs in the Ru/CNT catalyst.[25] The Ru/CNT with smaller Ru NPs showed higher catalytic activity and higher selectivity to CH_4. To compare the performance of RuFe/CNT catalysts at different Ru/Fe ratios, all the catalysts were prepared with almost the same particle size of ~3 nm. The selectivity to 1,2-PDO on Ru/CNT was only 22.1% (Table 3), indicating that the catalyst with smaller Ru NPs favors the C−C bond cleavage by forming CH_4. For the RuFe/CNT catalyst, however, the selectivity to 1,2-PDO was enhanced considerably. Taking the results of the formation of Ru−Fe alloys on the CNT surfaces into account, we have the conviction that the RuFe bimetallic NPs are beneficial for promoting C−O bond breakage but suppressing C−C bond cleavage.

The previous work also showed that, as compared to Ru/CNT, the Ru catalysts with AC, TiO_2, and Al_2O_3 as supports gave higher conversions of glycerol, but they favored production of CH_4 rather than 1,2-PDO and EG. The Ru/graphite catalyst showed higher selectivities to 1,2-PDO and EG, but its activity was much lower than the others.[25] As can be seen in Table 3, the performance of the AC-supported bimetallic RuFe catalyst was lower than the CNT-supported one under identical conditions. Therefore, the perfect alignment of lattices along the CNT axis and the curvature of graphite-like planes can bring about several novel properties to CNT, such as defect sites and functional groups on the surface, electrical conductivity, and chemical stability compared with traditional carriers.[34,35] These properties of CNT can be favorable for the electron transfer rates of reaction and the desorption of products, making it superior to other carriers supporting the same composition of RuFe.

The influence of reaction time is illustrated in Figure 6. Glycerol conversion increased as a function of reaction time and reached 100% after reaction for 24 h. Since the glycerol concentration had a significant effect on the conversion of glycerol in the glycerol hydrogenolysis,[5,10] the reaction appeared to be half over the first 5 h, whereas an additional 15 h or so was needed to reach completion, as a result. However, the selectivity to 1,2-PDO, EG, and CH_4 changed insignificantly with prolonged reaction time, implying that the hydrogenolysis of glycerol proceeded preferentially over that of 1,2-PDO and EG on the RuFe/CNT catalyst.

The stability of the RuFe/CNT catalyst was determined through consecutive recycling runs (Figure 7). Each run was controlled to perform for 12 h. After each experiment, the used catalyst was separated by filtration, dried at 383 K for 1 h, and reused in the next reaction. The recovery rate of the used catalyst was about 98−99%. The conversion of glycerol dropped gradually with the increase of recycling numbers for the Ru/CNT catalyst. Upon recycling, the selectivity to 1,2-PDO increased but that to EG decreased slightly. The decrease in glycerol conversion and the slight changes in selectivities could be attributed to the partial agglomeration of the Ru NPs on the catalyst surfaces, caused by high pressure and the liquid phase nature of the reaction. Over the Ru_2Fe_1/CNT catalyst, the conversion of glycerol remained almost constant, and the selectivity to 1,2-PDO and EG changed negligibly during the reuses. The XPS results showed that some Fe species are in the form of oxides on the periphery of RuFe bimetallic NPs on the CNT surfaces. These species could have merit for the stability of NPs. In other words, the stable structure and performance of the Ru_2Fe_1/CNT catalyst are largely due to the anchoring effect of iron oxides against the agglomerations of RuFe bimetallic NPs.

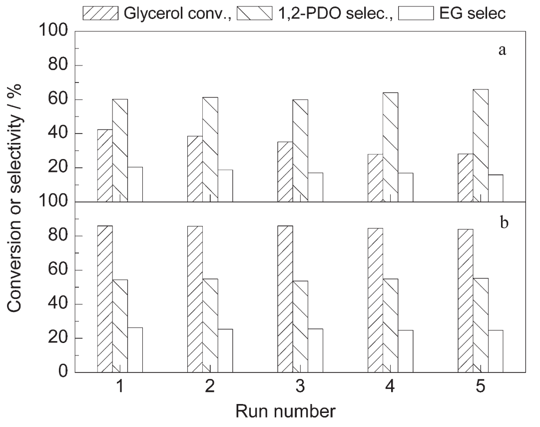

Figure 7. Recycling results of Ru/CNT and Ru_2Fe_1/CNT catalysts for glycerol hydrogenolysis: (a) Ru/CNT and (b) Ru_2Fe_1/CNT. Reaction conditions: time = 12 h, others are the same as in Table 3.

Therefore, the formation of the Ru/CNT and RuFe/CNT catalysts is outlined in Figure 8. The monometallic Ru/CNT catalyst with smaller Ru NPs showed a higher activity for the C−C bond cleavage, leading to higher selectivity to CH_4 but a lower one to 1,2-PDO. When the bimetallic RuFe/CNT catalyst was prepared with the appropriate Ru/Fe atomic ratio and a particle size similar to the Ru NPs in Ru/CNT, a higher selectivity to 1,2-PDO but a lower one to CH_4 was obtained. The selectivity to 1,2-PDO increased from 45.4% to 61.4% when the Ru/Fe atomic ratio decreased from 10/1 to 1/1. A portion of the Fe species were interacted with Ru moieties by forming the Ru−Fe alloys on the domain of Ru NPs. The amount of Ru−Fe alloys was increased slightly with the increase of Fe concentration. Other Fe species were most likely present on the catalyst surfaces in the forms of FeO and FeO_{1+x} ($0 < x < 0.5$), and they would exist on the periphery of RuFe bimetallic NPs. These iron oxide species having strong interactions with RuFe bimetallic NPs were vital for the stability of the catalyst structure during the catalytic runs. Nonetheless, excess iron oxides could cover and block the surfaces of RuFe bimetallic NPs, resulting in a drop in catalytic activity. As demonstrated in Table 3, the conversion of glycerol was ∼86.0% over the Ru_2Fe_1/CNT catalyst but dropped to ∼57.1% over Ru_1Fe_1/CNT, although the average size of bimetallic particles was same for each (∼3.0 nm).

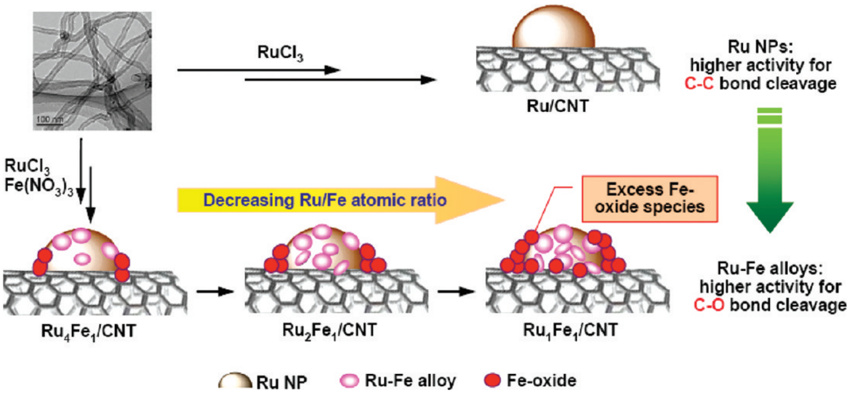

Figure 8. A schematic for preparation of Ru/CNT and RuFe/CNT catalysts and their catalytic behaviors in the hydrogenolysis of glycerol.

CONCLUSIONS

Selective hydrogenolysis of aqueous glycerol was performed over the RuFe/CNT catalysts to produce glycols. Superior performance with almost 100% conversion of glycerol and above 75% selectivity to glycols was obtained over the optimized RuFe/CNT catalyst under relatively mild conditions. This catalyst was structurally stable and showed excellent reusability.

Characteristic studies revealed that there were two kinds of Fe species during the reduction process: metallic Fe species interacted with Ru by forming Ru−Fe alloys in the domain of Ru NPs and iron oxide species FeO and FeO_{1+x} ($0 < x < 0.5$) on the periphery of the Ru domain. The high activity of the catalysts was essentially attributed to the synergistic effects of the formation of Ru−Fe alloys and the interactions between RuFe bimetallic NPs and iron oxides on the CNT surfaces. However, excess iron oxide species on the catalyst surfaces would block the activity.

ASSOCIATED CONTENT

Supporting Information. Curve fitting of XPS, HRTEM image of Ru/CNT catalyst and TEM images of some catalysts after reaction. This material is available free of charge via the Internet at http://pubs.acs.org.

AUTHOR INFORMATION

Corresponding Author

*(Y.Y.) Phone: +86-592-2181659. Fax: +86 592 2183047. E-mail: yzyuan@xmu.edu.cn. (K.A.) Phone, Fax: +86-11-706-9113. E-mail:askr@cat.hokudai.ac.jp.

ACKNOWLEDGMENT

We gratefully acknowledge the financial supports from the National Basic Research Program of China (No. 2011CBA00508), the National Natural Science Foundation of China (Nos. 20873108 and 20923004), the Program for Changjiang Scholars and Innovative Research Team in University (No. IRT1036), and the Cooperative Research Program of Catalysis Research Center, Hokkaido University (Grant No. 10B0043). Bondong Li was supported by the Japan Society for the Promotion of Science (JSPS) with its Education Program for Advanced Science and Technology 2009.

REFERENCES

(1) Huber, G. W.; Iborra, S.; Corma, A. *Chem. Rev.* **2006**, *106*, 4044–4098.

(2) Fernando, S.; Adhikari, S.; Chandrapal, C.; Murali, N. *Energy Fuels* **2006**, *20*, 1727–1737.

(3) Nakagawa, Y; Tomishige, K. *Catal. Sci. Technol.* **2011**, *1*, 179–190.

(4) Chaminand, J.; Djakovitch, L.; Gallezot, P.; Marion, P.; Pinel, C.; Rosier, C. *Green Chem.* **2004**, *6*, 359–361.

(5) Dasari, M. A.; Kiatsimkul, P.-P.; Sutterlin, W. R.; Suppes, G. J. *Appl. Catal., A* **2005**, *281*, 225–231.

(6) Huang, Z. W.; Cui, F.; Kang, H. X.; Chen, J.; Zhang, X. Z.; Xia, C. G. *Chem. Mater.* **2008**, *20*, 5090–5099.

(7) Werpy, T. A.; John, J.; Frye, G.; Zacher, A. H.; Miller, D. J. US Patent 6,841,085, 2005.

(8) Alvise, P.; Pietro, T. *Ind. Eng. Chem. Res.* **2005**, *44*, 8535–8537.

(9) Lahr, D. G.; Shanks, B. H. *J. Catal.* **2005**, *232*, 386–394.

(10) Miyazawa, T.; Kusunoki, Y.; Kunimori, K.; Tomishige, K. *J. Catal.* **2006**, *240*, 213–221.

(11) Miyazawa, T.; Koso, S.; Kunimori, K.; Tomishige, K. *Appl. Catal., A* **2007**, *329*, 30–35.

(12) Feng, J.; Fu, H.; Wang, J.; Li, R.; Chen, H.; Li, X. *J. Catal. Commun.* **2008**, *9*, 1458–1464.

(13) Balaraju, M.; Rekha, V.; Sai Prasad, P. S.; Prabhavathi Devi, B. L. A.; Prasad, R. B. N.; Lingaiah, N. *Appl. Catal., A* **2009**, *354*, 82–87.

(14) Kurosaka, T.; Maruyama, H.; Naribayashi, I.; Sasaki, Y. *Catal. Commun.* **2008**, *9*, 1360–1363.

(15) Maris, E. P.; Ketchie, W. C.; Murayama, M.; Davis, R. J. *J. Catal.* **2007**, *251*, 281–294.

(16) Maris, E. P.; Davis, R. J. *J. Catal.* **2007**, *249*, 328–337.

(17) Ma, L.; He, D. H.; Li, Z. P. *Catal. Commun.* **2008**, *9*, 2489–2495.

(18) Shimao, A.; Koso, S.; Ueda, N.; Shinmi, Y.; Furikado, I.; Tomishige, K. *Chem. Lett.* **2009**, *38*, 540–541.

(19) Shinmi, Y.; Koso, S.; Kubota, T.; Nakagawa, Y.; Tomishige, K. *Appl. Catal., B* **2010**, *94*, 318–326.

(20) Nakagawa, Y.; Shinmi, Y.; Koso, S.; Tomishige, K. *J. Catal.* **2010**, *272*, 191–194.

(21) Deniel, O. M.; DeLaRiva, A.; Kunkes, E. L.; Datye, A. K.; Dumesic, J. A.; Davis, R. J. *ChemCatChem* **2010**, *2*, 1107–1114.

(22) Amada, Y.; Koso, S.; Nakagawa, Y.; Tomishige, K. *ChemSusChem* **2010**, *3*, 728–736.

(23) Amada, Y.; Shinmi, Y.; Koso, S.; Kubota, T.; Nakagawa, Y.; Tomishige, K. *Appl. Catal., B* **2011**, *105*, 117–127.

(24) Stytsenko, V. D. *Appl. Catal., A* **1995**, *126*, 1–26.

(25) Wang, J.; Shen, S. H.; Li, B. D.; Lin, H. Q.; Yuan, Y. Z. *Chem. Lett.* **2009**, *38*, 572–573.

(26) Chen, P.; Zhang, H. B.; Lin, G. D.; Hong, Q.; Tsai, K. R. *Carbon* **1997**, *35*, 1495–1501.

(27) Taylor, K. C. *J. Catal.* **1975**, *38*, 299–305.

(28) Steen, E.; Prinsloo, F. F. *Catal. Today* **2002**, *71*, 327–334.

(29) Guerrero-Ruiz, A.; Sepúlveda-Escribano, A.; Rodríguez-Ramos, I. *Appl. Catal., A* **1992**, *81*, 81–100.

(30) Burch, R.; Hayes, M. J. *J. Catal.* **1997**, *165*, 249–261.

(31) Brundle, C. R.; Chuang, T. J.; Wandelt, K. *Surf. Sci.* **1977**, *68*, 459–468.

(32) Mahata, N.; Vishwanathan, V. *J. Catal.* **2000**, *196*, 262–270.

(33) Anderson, J. R. *Structure of Metallic Catalysts*; Academic Press: New York. 1975; p 296.

(34) Gong, K. P.; Chakrabarti, S.; Dai, L. M. *Angew. Chem., Int. Ed.* **2008**, *47*, 5446–5450.

(35) Zhang, J.; Liu, X.; Blume, R.; Zhang, A. H.; Schlögl, R.; Su, D. S. *Science* **2008**, *322*, 73–77.